Volume 5
Number 4
21 February 2024
Pages 1351–1758

Materials Advances

rsc.li/materials-advances

ISSN 2633-5409

ROYAL SOCIETY OF CHEMISTRY

PAPER
Toshio Naito *et al.*
Nearly three-dimensional Dirac fermions in an organic crystalline material unveiled by electron spin resonance

Materials Advances

ROYAL SOCIETY OF CHEMISTRY

PAPER

View Article Online
View Journal | View Issue

Cite this: *Mater. Adv.*, 2024, 5, 1492

Nearly three-dimensional Dirac fermions in an organic crystalline material unveiled by electron spin resonance†

Ryuhei Oka,[a] Keishi Ohara,[ab] Naoya Tajima,[c] Toshihiro Shimada[d] and Toshio Naito*[abe]

Received 30th August 2023,
Accepted 31st October 2023

DOI: 10.1039/d3ma00619k

rsc.li/materials-advances

Materials containing Dirac fermions (DFs) have unique electronic properties, and have been extensively studied. Electron spin resonance revealed that α-ET_2I_3 (ET = bis(ethylenedithio)-tetrathiafulvalene) at 1 bar contained a nearly three-dimensional DFs above ~100 K coexisting with standard fermions. The close charge-transfer ET–I_3 interactions account for temperature-sensitive three-dimensional (3D) band structures and temperature-independent resistivity behaviour. As 3D band structures cannot be depicted in a four-dimensional space, the analysis method proposed herein provides a general way to present important and easy-to-understand information of such band structures that cannot be obtained otherwise.

Introduction

Recently, a quantum state of matter called topological material has garnered considerable attention from a wide range of materials scientists.[1–7] There are many types of topological materials known to date. All of their unique physical properties originate from Dirac fermions (DFs) located around the Fermi levels and governing the electrical, magnetic, and optical properties, instead of the standard fermions (SFs) of electrons or holes in common materials. The SFs transform to DFs when they are accommodated in linearly dispersive parts of bands called Dirac cones (Fig. 1).[8] To understand the mechanism of such intriguing physical properties, the direct observation of DFs with their characteristic electronic properties is important. However, the direct observation is demanding, partly because some require high pressure (~12 000 bar, for example) to realise such band structures,[9–16] and partly because the direct observation of the band structures requires an extremely high accuracy (*e.g.*, a few meV) in energy. However, for observation, most measurements require larger energy of perturbation than a few meV and are performed at high temperatures (*T*s) to allow significant thermal excitation, both of which often prevent the unambiguous observation of the ground states of the DF systems. These experimental restrictions practically narrow down the available powerful tools for observation, such as angle-resolved photoemission spectroscopy (ARPES) and

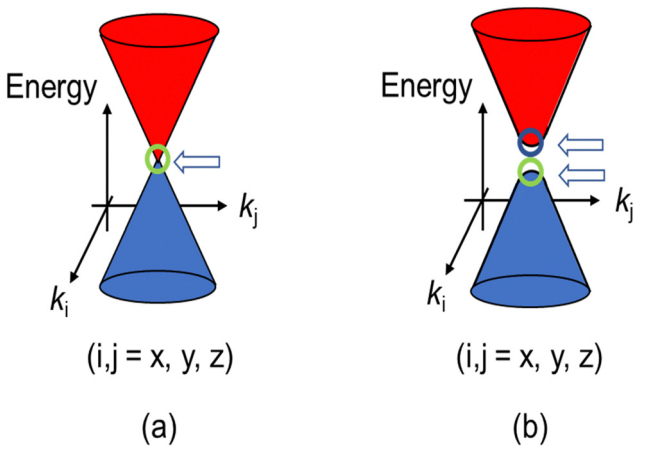

Fig. 1 (a) Schematic band structure of the Dirac cones. A close view of the band structure of a typical DF system, a zero-gap semiconductor, around a Weyl point indicated by the arrow. (b) Dirac cones with round apexes and with an energy gap between two Weyl points. The cases (a) and (b) correspond to $m = 0$ and $m \neq 0$, respectively in eqn (1). The energy gap between the two cones in (b) equals $2mc^2$ (a "mass gap").

[a] *Graduate School of Science and Engineering, Ehime University, Matsuyama 790-8577, Japan. E-mail: tnaito@ehime-u.ac.jp*
[b] *Research Unit for Development of Materials Development for Efficient Utilization and Storage of Energy (E-USE), Ehime University, Matsuyama 790-8577, Japan*
[c] *Department of Physics, Toho University, Funabashi, Chiba 274-8510, Japan*
[d] *Graduate School of Engineering, Hokkaido University, Kita 13, Nishi 8, Kita-ku, Sapporo 060-8628, Japan*
[e] *Geodynamics Research Center (GRC), Ehime University, Matsuyama 790-8577, Japan*

† Electronic supplementary information (ESI) available: Experimental details, the calculated band structure in the k_ak_b plane (Fig. S1), angle- and temperature-dependencies in the ESR spectra (Fig. S2), the parameters for the simulated ESR spectra (Tables S1–S16). See DOI: https://doi.org/10.1039/d3ma00619k

scanning tunnelling microscopy/spectroscopy (STM/STS) at extremely low *T*s (a few Kelvins or lower, for example).[17,18] Both observations are surface-sensitive and require an ultra-high vacuum, where the samples (single crystals) should be cleaved to expose atomically clean surfaces prior to the observation.

Meanwhile, some organic charge-transfer (CT) salts have been studied in terms of the DFs.[19–38] They include α-D_2I_3 (D = ET = bis(ethylenedithio)-tetrathiafulvalene, STF = bis(ethylenedithio)-diselenadithiafulvalene, and BETS = bis(ethylenedithio)-tetraselenafulvalene: Scheme 1).

In 2007–2008, the high-pressure phase (≥12 kbar) of α-ET_2I_3 was established as a DF system called zero-gap semiconductor (ZGS; Fig. 1(a)).[19–30] Recently, it has been argued that the related salts, α-STF_2I_3[31–35] and α-$BETS_2I_3$,[31,36–38] are also close to or belong to ZGSs based mainly on the band calculations. Their apparent advantage over other DF systems is that the DFs can be observed as bulk properties, such as electrical resistivity without any demanding pre-treatment for observation. The bulk properties originate from internal parts of condensed matters, which are protected to be intact by their own surfaces. Furthermore, the bulk sample can contain three-dimensional (3D) DF systems, which nanosheets such as graphene cannot contain. The difference in the system dimension generally provides qualitatively different physical properties.[39–41] However, most work on the organic DFs thus far has been focused on the two-dimensional (2D) ZGSs, which is the same feature that graphene and related nanosheets possess. Except for a limited range of *T*s, the electronic states of α-D_2I_3 at 1 bar remain rather unexplored, as they were speculated to be less relevant to ZGS. However, lack of experimentally detailed and systematic information on the electronic structures at 1 bar in these materials leaves important questions unanswered. For example, in previous papers, many molecular conductors were classified as ZGSs exclusively based on the *T*-independent resistivity (TIR) except for the calculated band structures, as if the observation of TIR should be the necessary and sufficient condition. However, there is no explanation as to why α-ET_2I_3 in the metallic phase (at 1 bar and $T > 135$ K) exhibits identical resistivity behaviour (the TIR) with that in the ZGS state of the same material ($P \geq 12$ kbar). Additionally, there is no explanation as to why most Weyl points in molecular conductors are located at general points in the reciprocal space, which are not associated with high symmetries for allowing the degeneracy between the two bands. These unanswered questions make it unclear which behaviour should be associated with the ZGS states. In our previous study, we proposed *T*-dependent band structures of α-D_2I_3 (ET = ET and BETS) (296–30 K) based on a first-principles calculation, and established their validity by comparing them with the observed electrical, magnetic, and optical properties.[42] Based on the study, we clarified that the carrier systems in these salts contain two kinds of fermions: SFs at the Fermi surfaces and DFs at different parts of the same bands with linear dispersions like Dirac cones. It should be noted that it never means that α-ET_2I_3 should be a ZGS at 1 bar, but means that it is a semiconductor with a separated pair of "round-apex Dirac cones" in the insulating phase (Fig. 1(b)). As a part of the thermally excited fermions (electrons and holes) that are located at the linear dispersive parts of the cones at some *T* range, they behave as DFs. With varying *T* at 1 bar, the band structures vary qualitatively and the dominant carrier system crosses over between the two kinds of fermions. The relationship between the two kinds of fermions in Fig. 1(a) and (b) is described by eqn (1),

$$E = \pm\sqrt{(\hbar ck)^2+(mc^2)^2} \quad (1)$$

where *E*, *c*, *k*, and *m* are the energy of fermions, the light velocity, wave vector of fermions, and effective mass of fermions, respectively.

Electron spin resonance (ESR) enables us direct observation of such DFs, distinguishing them from the coexisting SFs as different spin systems. Therefore, using ESR, the single crystals of α-D_2I_3 at 1 bar are the sample of choice for the observation of DFs, including how they originate from SFs or *vice versa*. In this work, we examined the ESR spectra of the single crystals of α-ET_2I_3 concerning magnetic-field-angle (θ)- and *T*-dependencies, which have unveiled the nearly 3D behaviour of DFs in this salt above ~100 K.

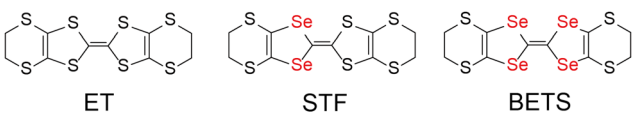

Scheme 1 Chemical structures of ET, STF, and BETS.

Results and discussion

The discussion thus far is qualitatively valid for three-dimensionally at any *T* and 1 bar in α-ET_2I_3 (Fig. 2). Thus, the molecular orbitals of the ET cations and I_3 anions are mixed in a complicated manner to form conduction and valence bands of α-ET_2I_3. This situation makes the discussion on the electronic properties more comprehensive based on the band structure compared to the crystal structure. Therefore, firstly, we will relate the conduction behaviour to the band structure features shared by the k_ak_c (Fig. 2) and k_ak_b (Fig. S1, ESI†) spaces, and then refer to supplementary features based on the crystal structure (Fig. 3). We will not repeat similar discussion on the band structures in the k_ak_b space (Fig. S1, ESI†), which are qualitatively similar to those in the k_ak_c space (Fig. 2). However, the band structure contains developing Dirac cones and narrowly recognisable Weyl points in the k_ak_b space, whilst the Dirac cones merged into a nodal line in the k_ak_c space. Thus, hereafter, we will refer to these Dirac-cone-related features as "linearly dispersive parts in the bands". At 296 K, the conducting properties are governed by two kinds of fermions mobile in a nearly 3D way (Fig. 2 and Fig. S1, ESI†): SFs (electrons at the Fermi surface in the 3D bands) and DFs (thermally excited electrons and holes at the linearly dispersive parts in the 3D bands). At 150 K, the Fermi level intersects with the top of the linearly dispersive parts of the second HOMO band in both k_ak_b (Fig. S1, ESI†) and k_ak_c spaces (Fig. 2), which means that the 3D DFs dominate the conduction at ~150 K. A metal (high-*T*

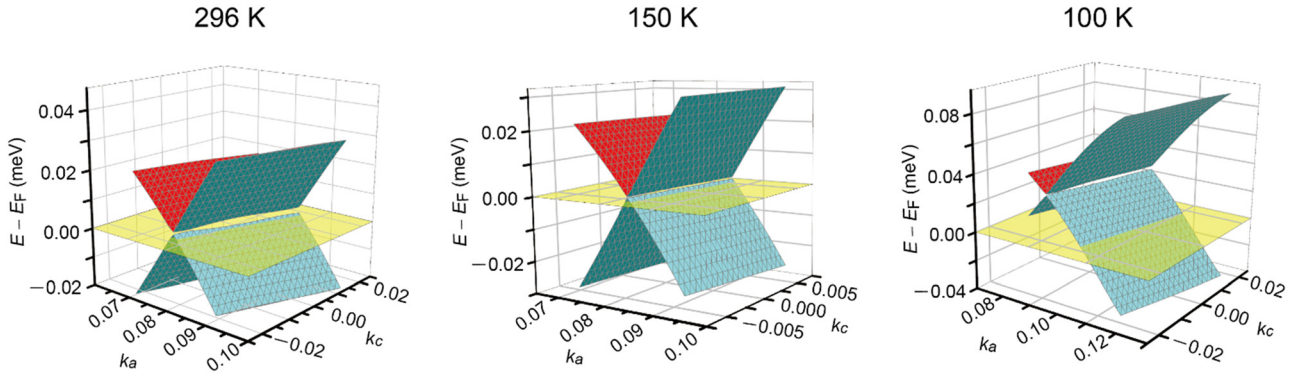

Fig. 2 Band structures near the Fermi level E_F in α-ET_2I_3 at 1 bar and 296, 150, and 100 K in the k_ak_c space. At each T, the Fermi level is shown by the half-transparent yellow plane. The green (front)/red (back) and blue (front)/green (back) curved surfaces respectively show a part of the top and the second HOMO bands. The corresponding figure (the band structures in the k_ak_b space at 296, 150, and 100 K) is shown in Fig. S1 in the ESI,† which also shows linearly dispersive parts in the band structure.

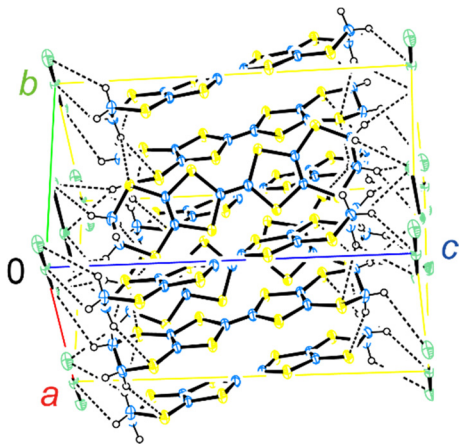

Fig. 3 Crystal structure of α-ET_2I_3. The blue, yellow, open, and green spheres indicate C, S, H, and I atoms, respectively. The broken lines indicate the (C−)H···I and (C−)H···S contacts that are shorter than the van der Waals distances (3.35 and 3.05 Å, respectively). At 296 K, a, b, and c = 9.17584(13), 10.79078(17), and 17.4193(3) Å, and α, β, and γ = 96.9633(13), 97.9521(13), and 90.8572(12)°, respectively.

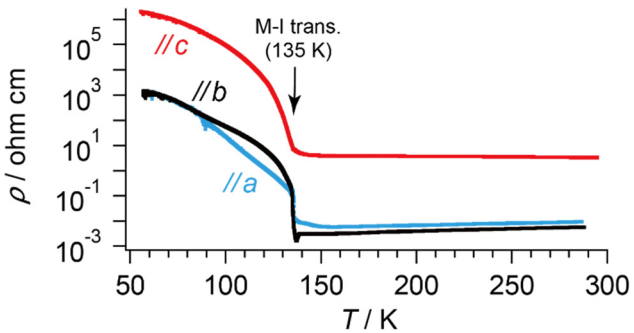

Fig. 4 T-dependent electrical resistivities of α-ET_2I_3 along each crystallographic axis. The values are identical at $T \approx$ 60–90 K along the a- and b-axes.

phase)–insulator (low-T phase) (M–I) transition occurs at 135 K in α-ET_2I_3. This causes the Fermi surface and the SFs to disappear simultaneously, and causes energy gaps to appear. The M–I transition allows for distinguishing the SFs and DFs in α-ET_2I_3. At 100 K, there are energy gaps of a few meV at the linearly dispersive parts in the k_ak_b space (Fig. S1, ESI†), which means that no SFs contribute to the conduction in the ab plane. On the other hand, the Fermi level intersects the lower band still at 100 K in the k_ak_c space (Fig. 2), which contradicts with the observed resistivity behaviour (Fig. 4). This inconsistency is probably attributable to stronger electron correlation[20,26,29,30] or a larger change in the effective charge of ET $(0.5 - \delta)$[42] than our calculation estimated. Consistently, the temperature dependence of resistivity ($\|b$) slightly varies at $T \leq$ 90–100 K (Fig. 4). The value of δ is T-dependent because it depends on the ET–I_3 CT interactions, which are based on a chemical equilibrium and thus are also T-dependent.[42] The assumption that the insulating (charge ordered) phase in α-ET_2I_3 ($T <$ 135 K) is not a simple band insulator is qualitatively consistent with the observed T-dependent activation energy in this phase.[9] Accordingly, thermally excited electrons and holes through the band gap around the linearly dispersive parts serve as carriers and behave as DFs at ∼100 K.

The crystal structure of α-ET_2I_3 is shown in Fig. 3.[42,43] The unit cell contains three (more precisely, two halves and a whole) independent ET species and two (halves of) independent I_3 species. At the M–I transition (T_{MI} = 135 K), the space group changes between $P\bar{1}$ (a high-T, metallic phase) and $P1$ (a low-T, insulating phase). There are two key features in the crystal structure, which are indispensable to uniquely realize the nearly 3D DFs. Firstly, the ET radical cations form 2D conduction sheets in the ab planes. Such network makes this salt a narrowly metallic conductor. Here, the phrase "a narrowly metallic conductor" is important. It indicates that the salt unambiguously belongs to the metals because it has a Fermi surface (Fig. 2 and Fig. S1, ESI†), satisfying the definition of metals. This is corroborated by the T-dependence of the resistivity ρ, $d\rho/dT > 0$, which is characteristic to the metals. However, the Fermi surface is extremely small (Fig. 2 and Fig. S1, ESI†), which indicates the metallic band structure should be unstable. This is also corroborated by the extremely small T-dependence of ρ in the metallic phase ($d\rho/dT \approx 0$ at $T \geq$ 135 K

at any direction in the unit cell) (Fig. 4), a conducting property also close to that of an insulator ($d\rho/dT < 0$). This underlying metal-instability promotes the Dirac-cone-like band structure formation, when the net charge of the ET cations changes by T-variation as explained next. Secondly, there are CT interactions between $ET^{+0.5}$ and I_3^- species, which vary the net charge of the ET cations ($ET^{+0.5} \rightarrow ET^{(0.5-\delta)+}$, $\delta \neq 0$), as follows. Firstly, they cause electron-doping from the I_3 anions to the ET cations. Then, they affect the metal-phase (in)stability, as they directly change the band filling and the Fermi energy. The electrical conduction is mainly based on the close ET–ET interactions in the *ab* planes supported by π–π overlaps between the highest occupied molecular orbitals (HOMOs) of ET. They are also singly occupied molecular orbitals (SOMOs) of ET, dominating the electronic properties. Furthermore, the ET–I_3 interactions extend the conduction pathway to the third direction (along the *c*-axis), which make the materials narrowly 3D metallic conductors as evidenced by the resistivity measurements (Fig. 4). Consistent with the abovementioned structural features, α-ET_2I_3 exhibited TIR-like ρ ($d\rho/dT \approx 0$) along the *a*-, *b*-, and *c*-axis at 300–135 K, which is an intermediate behaviour between metals ($d\rho/dT > 0$) and insulators ($d\rho/dT < 0$). However, this electrical behaviour does not necessarily indicate that the system belongs to the ZGSs, which also generally exhibit TIR in wide T ranges. Instead, the calculated band structure (Fig. 2) and the observed ESR spectra account for the observed electrical behaviour: α-ET_2I_3 at 1 bar has a closely related 3D band structure to ZGS at 1 bar (Fig. 1(b)) and TIR is a result of the combined contributions from SFs and DFs. The ratio of contributions varies with T in a complicated manner, which is revealed by the ESR analyses below.

Based on these structural and electrical properties, we discuss the ESR spectra mainly around T_{MI} = 135 K, as most noticeable changes in ESR are expected around T_{MI} to distinguish the SFs and DFs. The anisotropy was examined by rotating the single crystal around the *b*-axis from the *a*-axis ($\theta = 0^\circ$) toward the *c*-axis ($\theta \approx 98^\circ$), or around the *c*-axis from the *a*-axis ($\phi = 0^\circ$) toward the *b*-axis ($\phi \approx 91^\circ$) (Fig. 5 and 6). On rotating the single crystal around the *b*-axis, it should be noted that the ESR signals were weak and noisy independent of T and θ (Fig. 5(a) and (b)). The spectral measurements with rotation around the *c*-axis did not suffer from such weak intensities (Fig. 5(c) and (d)). This is not only because of the anisotropy in the resistivity (Fig. 4), but also because of complicated hyperfine (and possibly superhyperfine) structures (Fig. 6(a)) originating from each nuclear spin $I = 5/2$ on the four magnetically inequivalent iodine atoms in the unit cell. The hyperfine interactions split a single peak into many fine peaks.‡ In other

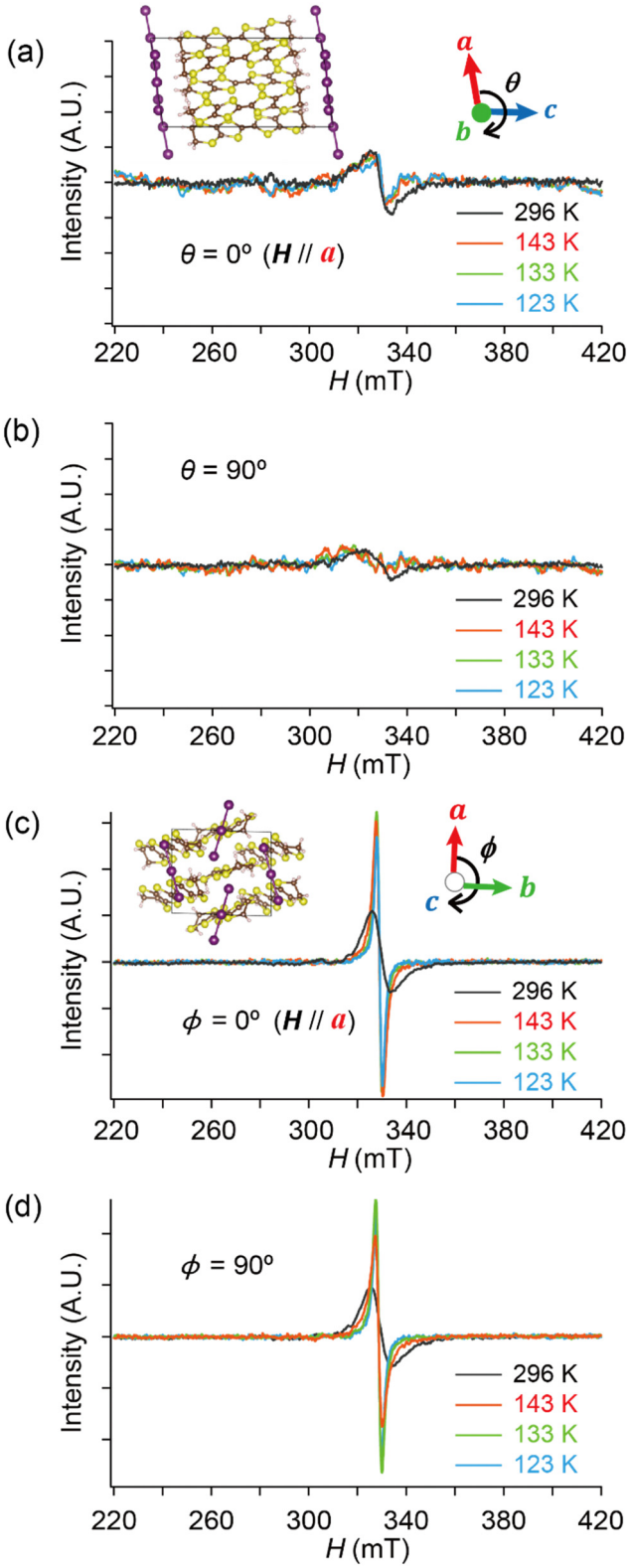

Fig. 5 Comparison of the T-dependent ESR spectra between different orientations (θ, ϕ = 0 and 90°) and between different rotation axes (*b*- and *c*-axes) of α-ET_2I_3. The sample (single crystal) was rotated around the *b*-axis (a), (b) and the *c*-axis (c), (d) with the indicated magnetic-field-angle θ and ϕ, respectively. $\boldsymbol{H} \| a$-axis when $\theta = 0^\circ$ and $\phi = 0^\circ$.

‡ For example, if the two crystallographically independent I_3 anions can be assumed to be identical in the hyperfine interactions and thus there are only two hyperfine constants regarding the I_3 anions, a single peak could be split into 65 peaks at most. If there are more kinds of hyperfine constants or if there are interactions between nuclear spins on the I atoms, additional peak splitting (super-hyperfine structures) occurs in the spectra, which makes each signal even more difficult to identify. Because of this complexity and many unidentified peaks, quantitative analyses like spectrum simulation were not performed.

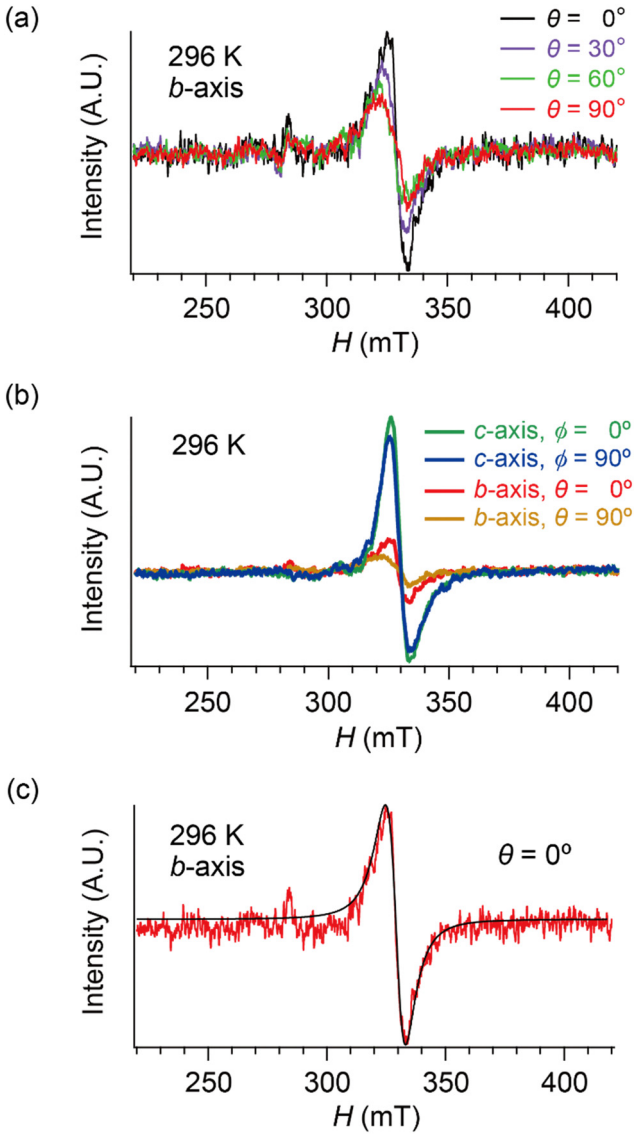

Fig. 6 Selected ESR spectra of α-ET_2I_3 (single crystal, 296 K). (a) Angle-dependence, θ = 0, 30, 60 and 90°, when the sample was rotated around the *b*-axis. (b) Comparison of the ESR spectra between different orientations (θ or ϕ) and between different rotation axes (*b*- or *c*-axes). (c) $\boldsymbol{H}\|a$-axis (θ = 0°) when the sample was rotated around the *b*-axis. Red and black curves show the observed and best-fit spectra, respectively. For the parameters of the simulated spectra, see Tables S1–S8 (ESI†). All the spectra in (b) were measured using the same single crystal under the identical measurement conditions, except for the crystal setting orientation.

words, to corroborate the ET–I_3 CT interactions, the *b*-axis rotation is the most favourable experimental condition for observing the spins on the I_3 anions.

Hereafter, we will discuss details of the main peak at ~330 mT (g = 2.006) observed when the sample was rotated around the *b*-axis (Fig. 5(a) and 6(c)). We will not repeat similar discussion on the spectra with the *c*-axis rotation (Fig. S2, ESI†), as the spectra with the *b*-axis rotation include necessary information for the following discussion. The lineshape and intensity were hardly dependent on T, and minimally affected by the M–I transition (Fig. 5(a)). However, they depended on the magnetic-field ($\boldsymbol{H}$)-angle θ (Fig. 6(a)), where $\theta = 0^\circ$ corresponded to the $\boldsymbol{H}\|a$-axis. When $\boldsymbol{H}$ was perpendicular to the *ab* planes (θ = 90°: Fig. 6(b)), the main peak was evidently less intensive than that of $\theta = 0^\circ$ (Fig. 6(a)). Our previous study indicated that there are CT interactions between ET and I_3 in α-ET_2I_3 with leaving spins on the I_3 anions.[42] Considering the arrangement of the I_3 anions in the unit cell (Fig. 3), the *b*-axis rotation includes the widest range of angles (~0 to ~90°) between the averaged principal axis of the I_3 anions and $\boldsymbol{H}$. Accordingly, the ESR spectra with the *b*-axis rotation should contain peaks assigned to the unpaired electrons on the iodine atoms in the $I_3^{(1-\delta)-}$ ($0 < \delta < 1$) anions. The nuclear spins on the inequivalent four iodine atoms in the two I_3 anions produce many highly complicated hyperfine and superhyperfine structures.‡§ Most of them may not be distinguished from noises. Accordingly, the main peak at ~330 mT should be an envelope of overlapped peaks of the delocalised spins.‡§ Although the delocalised spins in α-ET_2I_3 form a single spin system, the ESR peaks can be classified into three types based on the temporal locations of the spins during the resonance and based on the type of fermions: the signals assigned to the spins on the I_3 anions, those assigned to the SFs on the ET cations, and those assigned to the DFs on the ET cations. When the spins are on the I_3 anions, the finely split complicated peaks prevented the distinguishing of the type of fermions. Suggested by the observation of hyperfine structures, the spins on the I_3 anions exhibit more localised character than the other two types. Thus, they are more easily saturated under the high power radiation (P) of microwaves during ESR measurements than the other two types of spins.[42] Thus, above a certain value of P_{sat}, we can approximately suppress most hyperfine structures and resonance peaks assigned to the spins on the I_3 anions. In our previous work,[42] we found $P_{sat} \cong 9$ mW. In fact, the broad peak at ~330 mT under the measurement conditions in this study (P = 9 mW) was consistently deconvoluted in two peaks as shown below (Fig. 7 and 8). The intensity, lineshape, and g-value of the main peak were less dependent on θ than those of related organic conductors,[44,45] which indicates that the spin system is more isotropic around the *b*-axis than it appears from the crystal structure (Fig. 3). As the *b*-axis rotation includes both directions of the $\boldsymbol{H}\|$ and $\boldsymbol{H}\perp ab$ planes (2D conduction sheets), the spin system is close to 3D rather than 2D. It has recently revealed that α-ET_2I_3 also contains a 3D Dirac fermion system at high pressures.[46,47] Both experimental[46] and theoretical[47] studies corroborated that an interlayer coupling (ET–I_3-interaction) opens the energy gap between the Dirac cones as in Fig. 1(b), which is consistent with the present study. As the interlayer coupling is T-independent unless the crystal structure drastically changes, the energy gap between the Dirac cones remains through phase transitions, which is also consistent with the calculated band structures

§ The obtained g-values and linewidths are not consistent with those reported in ref. 44. As the observed spectra and other details on the ESR of α-ET_2I_3 are not described in their paper, the reason for inconsistency is not known.

(Fig. 2). The main peak remained below the M–I transition T_{MI} (135 K). The T-(in)dependence indicates that the major origin of the peak is the DFs at least at 123 K (the lowest T of measurements in this study) $\leq T <$ 135 K (T_{MI}). Because the band gap around where the Fermi surface was in the metallic phase is ~75–85 meV ($\approx$ 1000 K) in the insulating phase ($T <$ 135 K),[42,48] the contribution from thermally excited electrons and holes through this band gap, which are the SFs, can be ignored.

Next, we will distinguish the two spin systems: the SFs at the Fermi surfaces and the DFs at the linearly dispersive parts of the 3D bands. Using eqn (2), the fitting-analyses of the obtained ESR spectra revealed the angle (θ/rad) dependencies of spin susceptibility $\chi_s(\theta)$ and g-values $g(\theta)$.[49] Although the unit of angle θ was radian in the fitting, it is described in degree in the following figures (Fig. 7 and 8) for simplicity. $\chi_s(\theta)$ and $g_i(\theta)$ (i = x, y, and z) are based on the simulated spectra to exclude possible overlapped irrelevant peaks and noise. The parameters for the simulated spectra are summarised in Tables S1–S8 (ESI†).

$$\chi_s(\theta) \text{ or } g_i(\theta) = A\sin^2(a\theta + \delta_1) + B\sin^2(b\theta + \delta_2) + C \ (i = x, y, z) \quad (2)$$

where A and B are amplitudes, a and b are fitting parameters determining periods, δ_1 and δ_2 are phase shifts, and C is a constant. The fitting results are shown in Fig. 7(a) and (b), and the best-fit parameters are summarised in Tables S9–S16 (ESI†). The obtained g-values exhibit complicated θ-dependencies in the metallic phase (296 and 143 K), whilst highly symmetric and periodic behaviour in the insulating phase (123 K) (Fig. 7(a) and (b)), consistent with the fact that one of the spin systems (SFs as metallic carriers) disappeared below T_{MI} = 135 K. The consistency between the ESR spectra and M–I transition is discussed in more detail below.

First, we will discuss $g(\theta)$ in Fig. 7(a). If $g(\theta)$ is ideally 2D:

$$g_y(\theta) = g_x(\theta + \pi/2) \quad (3)$$

Then, based on eqn (2) and (3),

$$g_x(\theta) + g_y(\theta) = g_0\sin^2\theta + g_0\cos^2\theta = g_0. \quad (4)$$

where g_0 is the common amplitude of $g_x(\theta)$ and $g_y(\theta)$. Eqn (4) indicates that an ideal 2D (fourfold rotation symmetry) spin system exhibits a constant g-value when they are rotated around the symmetry axis, as was effectively observed in the ESR spectra in the ab plane (Fig. S2, ESI†). In other words, the deviation of θ-dependence from a constant g-value is a sensitive measure of anisotropy in the rotation symmetries. Based on the discussion thus far, the complicated θ- and T-dependencies of the g-values, g_x, g_y, and g_z, (Fig. 7(a)) indicate band re-shaping and coexistence of DFs and SFs at 296–133 K (the metallic phase). Particularly, the complicated θ-dependence indicates a fractional difference in phase shifts between δ_1 and δ_2 in eqn (2) (Tables S9–S16, ESI†). This indicates that the two spins systems, DFs and SFs, are located at different parts with different anisotropies in the band. At 123 K, where only the (thermally activated) DFs effectively remain in the spin system, all of the g-values, g_x, g_y, and g_z, exhibit a clear twofold rotation symmetry. This is consistent with previous work[26,42] and with the following discussion on the rotation symmetries of $\chi_s(\theta)$ (Fig. 7(b)).

Next, we will discuss $\chi_s(\theta)$ in Fig. 7(b). After deconvolution using eqn (2), it should be noted that the relationship between $\chi_s(\theta)$ and the amplitude at θ in each component (A or B) is indicated by eqn (5) and (6), respectively.

$$(\text{Component A})|I_A(\theta)| \equiv \sqrt{\chi_{s,A}(\theta)} \propto \sqrt{|A|}\sin(a\theta + \delta_1) \quad (5)$$

$$(\text{Component B})|I_B(\theta)| \equiv \sqrt{\chi_{s,B}(\theta)} \propto \sqrt{|B|}\sin(b\theta + \delta_2) \quad (6)$$

where $\chi_{s,A}(\theta)$ and $\chi_{s,B}(\theta)$ indicate the contributions of $\chi_s(\theta)$ in the A and B components, respectively, and $I_A(\theta)$ and $I_B(\theta)$ are the ESR signal intensities of the A and B components, respectively. It should be noted that the periods of $I_A(\theta)$ and $I_B(\theta)$ are described by the sine functions in eqn (5) and (6), respectively. Meanwhile, the periods of $\chi_{s,A}(\theta)$ and $\chi_{s,B}(\theta)$ are described by the square of the sine functions, as shown in eqn (2). Therefore, the periods of $\chi_{s,A}(\theta)$ and $\chi_{s,B}(\theta)$ are the half of $I_A(\theta)$ and $I_B(\theta)$, respectively. Thus, Fig. 7(b) indicates that $I_A(\theta)$ and $I_B(\theta)$ exhibit onefold and twofold rotation symmetries around the b-axis, respectively, at 296, 143, and 123 K. Similarly, Fig. 7(b) indicates that $I_A(\theta)$ and $I_B(\theta)$ exhibit onefold and fourfold rotation symmetries, respectively, at 133 K. Notably, regarding component A in each panel of Fig. 7(b), the rotation period (both a and δ_1 in eqn (2)) remains almost constant at 296–123 K. In contrast, component B exhibits a half (at 296, 143 K and 123 K) or a quarter (at 133 K) period of that of component A. As the period indicates the symmetry around the rotation axis, a shorter period implies a higher symmetry around the axis. The rotation symmetries coincide with the local symmetries of the band structure (in the k_ak_b or k_ak_c space), where the spins are located.¶ For example, the shapes of the sections of the band structure at the Fermi surfaces in the k_ak_b space are approximately ovals (Fig. S1, ESI†), whilst those around the Weyl points are nearly circles (Fig. S1, ESI†). Thus, in the k_ak_b space, the local symmetry is higher around the Weyl points than that around the Fermi surfaces. Accordingly, the shorter period wave (component B) is assigned to the DFs. Since it is impossible to depict the 3D band structures in a four-dimensional space, the thus-obtained information is important, which can be applied to other spin systems. The non-centrosymmetric (onefold rotation symmetry) feature of component A (SFs) is noteworthy. Although the non-centrosymmetric feature is shared by the crystal structure in the insulating phase (space group $P1$), it is not due to fluctuation of the insulating phase ($T <$ 135 K): the onefold rotation symmetry of component A constantly occurs at 296–123 K.

Here, we will make a brief comment on the consistency between $g(\theta)$ (Fig. 7(a)) and $\chi_s(\theta)$ (Fig. 7(b)) regarding the local

¶ It should be noted that the local symmetries at particular points in the band structure are independent of the crystallographic symmetry (the space group).

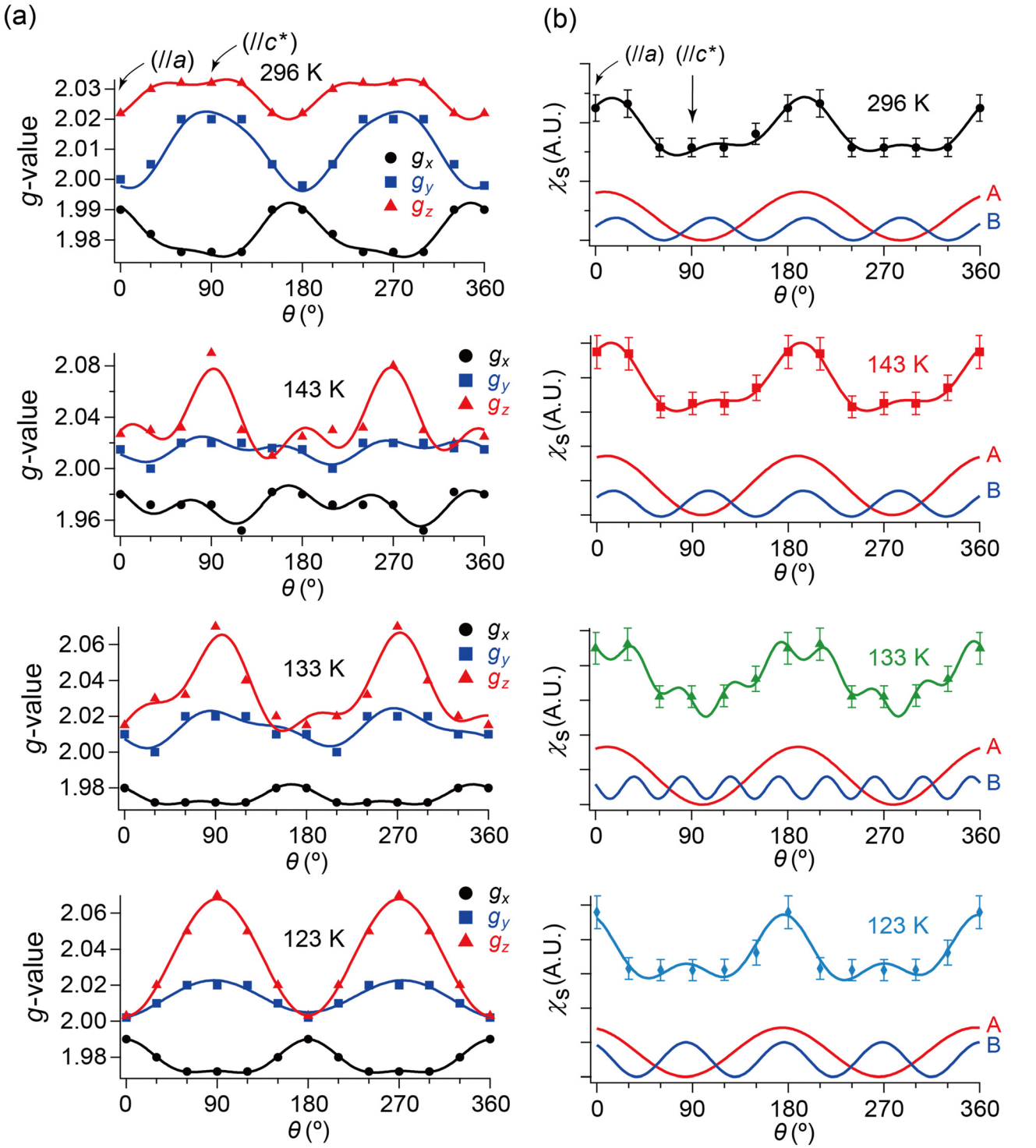

Fig. 7 θ- and T-dependencies of (a) g-values and (b) spin susceptibility χ_s of the ESR spectra when the single crystal was rotated around the b-axis. In each panel of (a), the three curves consist of the data from the simulated spectra with the best-fitting curves using eqn (2). Although the unit of angle θ was radian in the fitting, it is described in degree in this figure. The subscripts x, y and z of the g-values approximately indicate the following directions: (x, y) ≈ (a, b) or (b, a), and z ≈ c-axis. Whether (x, y) ≈ (a, b) or (b, a) could not be determined based on the ESR data. In each panel of (b), the bottom two curves indicate the fitting components to the top curve corresponding to the first (A) and second (B) terms in eqn (2), respectively. The obtained parameters are summarised in Tables S9–S16 (ESI†).

rotation symmetries of DFs and SFs. In the metallic phase (296–133 K), the complicated θ-dependences in both $g(\theta)$ and $\chi_s(\theta)$ are consistent with each other in that they both exhibit nearly twofold rotation symmetries. The onefold symmetry of SFs derived from $\chi_s(\theta)$ at 296–123 K is almost twofold symmetry based on the calculated band structures around the Fermi

surfaces (Fig. 2 and Fig. S1, ESI†). Thus, the SFs (component A) contribution to $g(\theta)$ should be approximately twofold like that of the DFs (ccomponent B), which was observed at 296–123 K as an overlap pattern of two waves with twofold symmetries with different phase shifts (Fig. 7(a) and Tables S9–S11, ESI†). Particularly at 123 K, the contribution of the SFs to $g(\theta)$ and $\chi_s(\theta)$ are negligible compared with the (thermally activated) DFs because of the M–I transition, as is discussed below.

A nearly 3D band structure based on the ET–ET and ET–I_3 interactions is obtained by combining our present (Fig. 2, the k_ak_c space) and previous[42] (Fig. S1, ESI† the k_ak_b space) band structures, and is supported by the observed 3D metallic T-dependence of the resistivity (Fig. 4).

Now, we clarify how DFs revolve with the band reshaping and temperature variation. As a coarse approximation, here we assume that the relaxation times in the ESR of SFs and DFs should be comparable to each other.‖ Then, one can roughly estimate the ratio between the numbers of SFs and DFs at T and θ based on the amplitudes of the two components, A and B (Fig. 8). At 296 K (the metallic phase) and 123 K (the insulating phase), the SFs (corresponding to A) dominate in number, but only in limited directions (Fig. 8(a)). Fig. 8(a) and (b) show that the DFs increase with decreasing T. At 143 K, the DFs become comparable to the SFs in number ($A/B \approx 1$) at practically all θ (Fig. 8(b)). This indicates that the DFs form a 3D system in the $k_ak_bk_c$ space, considering the b-axis rotation includes both directions of $\boldsymbol{H}\|$and $\boldsymbol{H}\perp ab$ planes (2D conduction sheets). The value of θ where A/B becomes maximum, θ_{max}, clearly shifts with T. This manifests how the SFs turn into the DFs: the DFs continuously increase with decreasing T and with change of the band structure. The transformation between DFs and SFs exhibited complicated T-dependence. In the middle of the M–I transition (133 K: green curves in Fig. 8(b)), the carrier system exhibited both features of θ-dependence in A/B at 296 K (black) and 143 K (red). This is noteworthy, as the θ-dependence at 296 K (black) was once averaged out at 143 K (red) and reproduced at 133 K (green). Finally, the values of θ_{max} are different between 296 K and 123 K, although the rotation symmetry is retained (Fig. 8(a) and (b)). Such complicated T-dependence of the band structure is explained as follows. The entire band structure is cooperatively governed by the ET–ET and ET–I_3 interactions at 296–123 K. Additionally, the number of carriers is T-dependent, but always small at all Ts in this salt, whether they are SFs or DFs. Thus, to lower the Gibbs energy of the electronic and lattice system, the interactions deform the smallest part of the band to be a cone or similar shapes toward the lower energy, where the carriers are accommodated. The number of carriers depends on T-sensitive ET–I_3 CT interactions. Such a subtle balance in energy based on the chemical equilibrium in the ET–I_3-redox reaction in the solid state is responsible for causing the observed complicated T-dependence and three-dimensionality in the "DF-SF equilibrium".

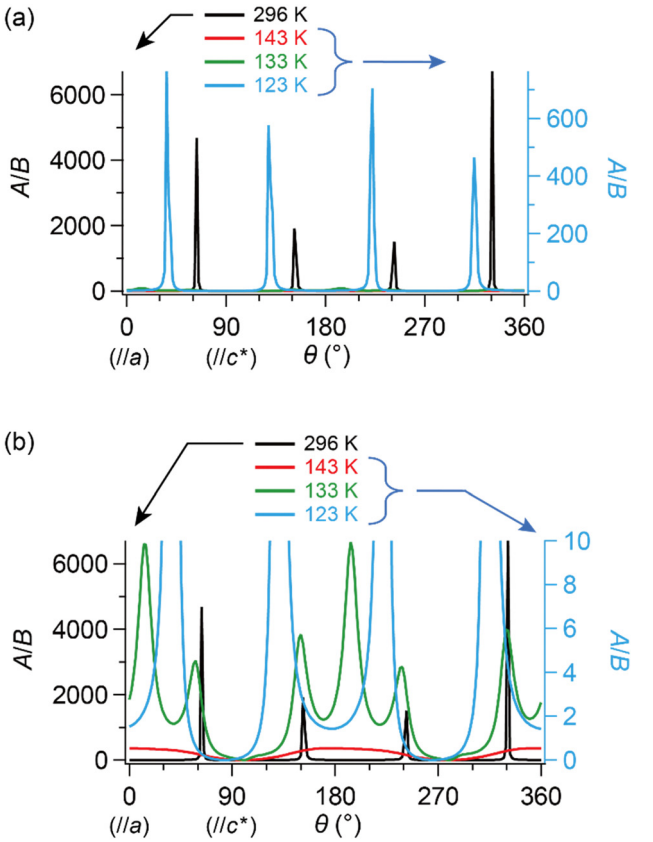

Fig. 8 θ- and T-dependencies of the ratio of amplitudes in components A and B in eqn (2), A/B, which approximately correlates with the number ratio between SFs and DFs, N_{SF}/N_{DF}. The single crystal was rotated around the b-axis, where $\theta = 0°$ corresponds to $\boldsymbol{H}\|a$-axis. (a) Entire and (b) enlarged view. It should be noted that both curves corresponding to 143 K (red) and 133 K (green) almost overlap with the horizontal axis in (a). Although the unit of angle θ was radian in the fitting, it is described in degree in this figure.

In summary, the coexisting components A and B at 296–123 K revealed by the ESR spectra demonstrated that the nearly 3D DFs are present at 296–123 K. The complicated T- and θ-dependencies of the two components are consistent with our band calculations indicating the T-dependent formation of the DFs.

Experimental

Selected information on materials, methods, and calculations are described below. Other details are described in ESI.†

Materials

The single crystals were prepared following the reported procedure.[42,43] Prior to the physical property measurements, all single crystals were checked by the X-ray oscillation

‖ Generally, the ESR signal intensity is not simply proportional to the number of unpaired electrons, when the signal originates from different kinds of electrons with different relaxation times. The Dirac electrons are generally considered to exhibit unusual short relaxation times in linearly dispersive parts of bands around the Fermi energies. However, it should not be assumed that they also exhibit unusual short relaxation times when they are photoexcited to parabolic or cosine bands across band gaps. They may behave as SFs in such non-linearly dispersive bands. Thus, our assumption on the relaxation times of DFs and SFs in ESR should be examined *via* further studies in the future.

photographs in terms of the crystal quality and orientation of crystallographic axes.

Band structure calculation

The electronic band structures were calculated using the Vienna *Ab initio* Simulation Package (VASP),[50] similarly to our previous work.[42] The PBE functional[51] was used along with the augmented plane wave method. Crystal structures derived from the X-ray diffraction experiments in our previous work[42] were used, and no structure optimization was performed. The structure at 150 K was provided by Prof. H. Sawa (Nagoya University, Japan). The atomic parameters used in the calculation are submitted as cif files in ESI.†

Electrical resistivity measurements

The electrical resistivities along the *a*-, *b*- and *c*-axes of the α-ET_2I_3 single crystals were measured by a standard four-probe method, where the four electrical leads were attached to align along the crystallographic axes. For the *c*-axis resistivity measurements, either side of the most developed face (the *ab* plane) of the platelet crystals was attached with two leads, and the constant current flew from one side to the other. Carbon paste and gold wires (15 μm in the diameter) were used as the electrical contacts. A commercially available VTI cryostat (CRYOGENIC) inserted with a homemade probe was used. The current source and the voltameter were Model 6221 AC and DC Current Source (KEITHLEY) and Model 2182A Nanovoltmeter (KEITHLEY), respectively.

ESR spectra measurements

The ESR spectra of the X band (9.3 GHz) were measured using the single crystals of α-D_2I_3 at 120–300 K with the JEOL JES-FA100. The single crystal was mounted on a Teflon piece settled with a minimal amount of Apiezon N grease, and sealed in a 5 mm-diameter quartz sample tube in a low-pressure (∼20 mmHg) helium atmosphere. The background signals were measured prior to the sample measurement under conditions identical to those of the samples, and the resultant spectra were subtracted from the raw sample spectra. The microwave power, *Q*-values, time constant, sweep time, modulation, and its amplitude were 9 mW, 4700–8200, 0.03 s, 1 min, 100 kHz, and 2 mT, respectively. Here, the *Q*-values are the factors indicating the resonance specification of the cavity, and are defined as the ratio between the energy stored in the cavity and that consumed inside the cavity. The magnetic field was corrected by a Gauss meter (JEOL NMR Field Meter ES-FC5) at the end of every measurement. The temperature was controlled using a continuous flow-type liquid N_2 cryostat with a digital temperature controller (JEOL). The temperature variation did not exceed ± 0.5 K during the field sweep. The cooling rate was −10 K min^{-1}. No hysteretic behaviour was observed in the ESR spectra between the heating and cooling processes.

Conclusions

Generally, the conducting properties are qualitatively sensitive to the dimension of the electronic systems. Additionally, the DF systems of any dimension (2D or 3D) often exhibit conducting behaviour that SFs do not exhibit under any condition. Using ESR, we identified nearly 3D DF systems underlying in α-ET_2I_3 at 1 bar. Additionally, the ratio between the numbers of SF and DF anisotropically depends on *T*. The crystalline materials with well-defined stoichiometries containing DFs are scarce, let alone the 3D DFs. Even more scarce are the fermions, which sensitively and reversibly transform themselves between DFs and SFs by varying *T* at 1 bar: a practical condition enabling various experiments. This work has established that α-ET_2I_3 has both features: a nearly 3D fermion system with a well-defined stoichiometry, being reversibly interconvertible between SFs and DFs by varying *T* at 1 bar. Such a flexible character of the electronic system is an evident advantage of conducting materials based on the weak van der Waals interactions, namely the organic conductors. The findings here will accelerate both theoretical and experimental studies on the DFs and their characteristic electronic properties.

Author contributions

T. N. contributed to the conceptualization, resources, funding acquisition, project administration, supervision, methodology, original draft writing, review, and editing. K. O. contributed to the formal analysis and resources. R. O., T. S. and N. T. performed the investigation and validation. R. O., N. T., T. S. and T. N. collaborated in the visualization.

Conflicts of interest

There are no conflicts to declare.

Acknowledgements

The authors are grateful to Prof. H. Sawa (Nagoya University) for providing the atomic coordinates of α-ET_2I_3 at 150 K. We would like to acknowledge the assistance provided by Dr S. Mori and Ms R. Konishi (ADRES, Ehime University) in the X-ray structural analyses. This work was partially funded by a Grant-in-Aid for Challenging Exploratory Research (18K19061) and a Grant-in-Aid for Scientific Research (B) (22H02034) of JSPS, the Iketani Science and Technology Foundation (ISTF; 0331005-A), the Research Grant Program of the Futaba Foundation, CASIO Science Promotion Foundation, an Ehime University Grant for Project for the Promotion of Industry/University Cooperation, and the Canon Foundation (Science and Technology that Achieve a Good Future).

Notes and references

1 W. Ko, Z. Gai, A. A. Puretzky, L. Liang, T. Berlijn, J. A. Hachtel, K. Xiao, P. Ganesh, M. Yoon and A.-P. Li, *Adv. Mater.*, 2023, **35**, 2106909.

2 J. Liu and T. Hesjedal, *Adv. Mater.*, 2023, **35**, 2102427.
3 S. Jana, A. Bandyopadhyay, S. Datta, D. Bhattacharya and D. Jana, *J. Phys.: Condens. Matter*, 2022, **34**, 053001.
4 M. M. Sharma, P. Sharma, N. K. Karn and V. P. S. Awana, *Supercond. Sci. Technol.*, 2022, **35**, 083003.
5 J.-X. Yin, B. Lian and M. Z. Hasan, *Nature*, 2022, **612**, 647.
6 Y. Lei, T. Zhang, Y.-C. Lin, T. Granzier-Nakajima, G. Bepete, D. A. Kowalczyk, Z. Lin, D. Zhou, T. F. Schranghamer, A. Dodda, A. Sebastian, Y. Chen, Y. Liu, G. Pourtois, T. J. Kempa, B. Schuler, M. T. Edmonds, S. Y. Quek, U. Wurstbauer, S. M. Wu, N. R. Gravin, S. Das, S. P. Dash, J. M. Redwing, J. A. Robinson and M. Terrones, *ACS Nanosci. Au*, 2022, **2**, 450.
7 H. Xue, Y. Yang and B. Zhang, *Nat. Rev. Mater.*, 2022, **7**, 974.
8 A. H. Castro Neto, F. Guinea, N. M. R. Peres, K. S. Novoselov and A. K. Geim, *Rev. Mod. Phys.*, 2009, **81**, 109.
9 N. Tajima, S. Sugawara, M. Tamura, Y. Nishio and K. Kajita, *J. Phys. Soc. Jpn.*, 2006, **75**, 051010.
10 N. Tajima, S. Sugawara, M. Tamura, R. Kato, Y. Nishio and K. Kajita, *EPL*, 2007, **80**, 47002.
11 N. Tajima, R. Kato, S. Sugawara, Y. Nishio and K. Kajita, *Phys. Rev. B: Condens. Matter Mater. Phys.*, 2012, **85**, 033401.
12 K. Kajita, Y. Nishio, N. Tajima, Y. Suzumura and A. Kobayashi, *J. Phys. Soc. Jpn.*, 2014, **83**, 072002.
13 N. Tajima, *Crystals*, 2018, **8**, 126.
14 T. Tani, N. Tajima and A. Kobayashi, *Crystals*, 2019, **9**, 212.
15 R. Kobara, S. Igarashi, Y. Kawasugi, R. Doi, T. Naito, M. Tamura, R. Kato, Y. Nishio, K. Kajita and N. Tajima, *J. Phys. Soc. Jpn.*, 2020, **89**, 113703.
16 T. Naito, *Crystals*, 2021, **11**, 838.
17 N. P. Amitage, E. J. Mele and A. Vishwanath, *Rev. Mod. Phys.*, 2018, **90**, 015001.
18 I. Crassee, R. Sankar, W.-L. Lee, A. Akrap and M. Orlita, *Phys. Rev. Mater.*, 2018, **2**, 120302.
19 A. Kobayashi, Y. Suzumura and H. Fukuyama, *J. Phys. Soc. Jpn.*, 2008, **77**, 064718.
20 M. Hirata, K. Ishikawa, K. Miyagawa, K. Kanoda and M. Tamura, *Phys. Rev. B: Condens. Matter Mater. Phys.*, 2011, **84**, 125133.
21 Y. Suzumura and A. Kobayashi, *J. Phys. Soc. Jpn.*, 2011, **80**, 104701.
22 Y. Suzumura and A. Kobayashi, *Crystals*, 2012, **2**, 266.
23 M. Monteverde, M. O. Goerbig, P. Auban-Senzier, F. Navarin, H. Henck, C. R. Pasquier, C. Mézière and P. Batail, *Phys. Rev. B: Condens. Matter Mater. Phys.*, 2013, **87**, 245110.
24 K. Miyagawa, Y. Sata, T. Taniguchi, M. Hirata, D. Liu, M. Tamura and K. Kanoda, *J. Phys. Soc. Jpn.*, 2016, **85**, 073710.
25 G. Matsuno, Y. Omori, T. Eguchi and A. Kobayashi, *J. Phys. Soc. Jpn.*, 2016, **85**, 094710.
26 M. Hirata, K. Ishikawa, K. Miyagawa, M. Tamura, C. Berthier, D. Basko, A. Kobayashi, G. Matsuno and K. Kanoda, *Nat. Commun.*, 2016, **7**, 12666.
27 D. Liu, K. Ishikawa, R. Takehara, K. Miyagawa, M. Tamura and K. Kanoda, *Phys. Rev. Lett.*, 2016, **116**, 226401.
28 R. Beyer, A. Dengl, T. Peterseim, S. Wackerow, T. Ivek, A. V. Pronin, D. Schweitzer and M. Dressel, *Phys. Rev. B*, 2016, **93**, 195116.
29 M. Hirata, K. Ishikawa, G. Matsuno, A. Kobayashi, K. Miyagawa, M. Tamura, C. Berthier and K. Kanoda, *Science*, 2017, **358**, 1403.
30 M. Hirata, A. Kobayashi, C. Berthier and K. Kanoda, *Rep. Prog. Phys.*, 2021, **84**, 036502.
31 K.-I. Hiraki, S. Harada, K. Arai, Y. Takano, T. Takahashi, N. Tajima, R. Kato and T. Naito, *J. Phys. Soc. Jpn.*, 2011, **80**, 014715.
32 T. Naito, R. Doi and Y. Suzumura, *J. Phys. Soc. Jpn.*, 2020, **89**, 023701.
33 T. Naito and R. Doi, *Crystals*, 2020, **10**, 270.
34 T. Naito and Y. Suzumura, *Crystals*, 2022, **12**, 346.
35 Y. Suzumura and T. Naito, *J. Phys. Soc. Jpn.*, 2022, **91**, 064701.
36 D. Ohki, K. Yoshimi and A. Kobayashi, *Phys. Rev. B*, 2020, **102**, 235116.
37 T. Tsumuraya and Y. Suzumura, *Eur. Phys. J. B*, 2021, **94**, 17.
38 S. Kitou, T. Tsumuraya, H. Sawahata, F. Ishii, K.-I. Hiraki, T. Nakamura, N. Katayama and H. Sawa, *Phys. Rev. B*, 2021, **103**, 035135.
39 T. Naito and Y. Fukuda, *Phys. Chem. Chem. Phys.*, 2022, **24**, 4147.
40 S. Das and V. Jayaraman, *Prog. Mater. Sci.*, 2014, **66**, 112.
41 M. Dressel, *Naturwissenschaften*, 2007, **94**, 527.
42 T. Naito, R. Oka, K. Ohara, K. Konishi, I. Yamane and T. Shimada, *Magnetochemistry*, 2023, **9**, 153.
43 K. Bender, I. Hennig, D. Schweitzer, K. Dietz, H. Endres and H. J. Keller, *Mol. Cryst. Liq. Cryst.*, 1984, **108**, 359.
44 T. Sugano, G. Saito and M. Kinoshita, *Phys. Rev. B: Condens. Matter Mater. Phys.*, 1986, **34**, 117.
45 E. L. Venturini, L. J. Azevedo, J. E. Schirber, J. M. Williams and H. H. Wang, *Phys. Rev. B: Condens. Matter Mater. Phys.*, 1985, **32**, 2819.
46 N. Tajima, Y. Kawasugi, T. Morinari, R. Oka, T. Naito and R. Kato, *J. Phys. Soc. Jpn.*, 2022, **92**, 013702.
47 T. Morinari, *J. Phys. Soc. Jpn.*, 2021, **90**, 104709.
48 T. Ivek, B. Korin-Hamzić, O. Milat, S. Tomić, C. Clauss, N. Drichko, D. Schweitzer and M. Dressel, *Phys. Rev. B: Condens. Matter Mater. Phys.*, 2011, **83**, 165128.
49 T. Nakamura, T. Nobutoki, T. Takahashi, G. Saito, H. Mori and T. Mori, *J. Phys. Soc. Jpn.*, 1994, **63**, 4110.
50 G. Kresse and J. Hafner, *Phys. Rev. B: Condens. Matter Mater. Phys.*, 1993, **47**, 558.
51 V. N. Mochalin, O. Shenderova, D. Ho and Y. Gogotsi, *Nat. Nanotechnol.*, 2012, **7**, 11.